*Aerosol Science and Technology*, 46:804–817, 2012
Copyright © American Association for Aerosol Research
ISSN: 0278-6826 print / 1521-7388 online
DOI: 10.1080/02786826.2012.663948

# Soot Particle Aerosol Mass Spectrometer: Development, Validation, and Initial Application

**T. B. Onasch,[1,2] A. Trimborn,[1,3] E. C. Fortner,[1] J. T. Jayne,[1] G. L. Kok,[4]**
**L. R. Williams,[1] P. Davidovits,[2] and D. R. Worsnop[1]**
[1]*Aerodyne Research Inc., Billerica, Massachusetts, USA*
[2]*Boston College, Chestnut Hill, Massachusetts, USA*
[3]*AeroMegt, Hilden, Germany*
[4]*Droplet Measurement Technologies, Boulder, Colorado, USA*

**The Soot Particle Aerosol Mass Spectrometer (SP-AMS) was developed to measure the chemical and physical properties of particles containing refractory black carbon (rBC). The SP-AMS is an Aerodyne Aerosol Mass Spectrometer (AMS) equipped with an intracavity laser vaporizer (1064 nm) based on the Single Particle Soot Photometer (SP2) design, in addition to the resistively heated, tungsten vaporizer used in a standard AMS. The SP-AMS can be operated with the laser vaporizer alone, with both the laser and tungsten vaporizers, or with the tungsten vaporizer alone. When operating with only the laser vaporizer, the SP-AMS is selectively sensitive to laser-light absorbing particles, such as ambient rBC-containing particles as well as metal nanoparticles, and measures both the refractory and nonrefractory components. When operated with both vaporizers and modulating the laser on and off, the instrument measures the refractory components of absorbing particles and the nonrefractory particulate matter of all sampled particles. The SP-AMS design, mass spectral interpretation, calibration, and sensitivity are described. Instrument calibrations yield a sensitivity of greater than 140 carbon ions detected per picogram of rBC mass sampled, a 3$\sigma$ detection limit of less than 0.1 $\mu$g·m$^{-3}$ for 60 s averaging, and a mass-specific ionization efficiency relative to particulate nitrate of 0.2 ± 0.1. Sensitivities were found to vary depending upon laser-particle beam overlap. The utility of the instrument to characterize ambient rBC aerosol is demonstrated.**

## 1. INTRODUCTION

Black carbon-containing particles are generated in the incomplete combustion of fossil fuels, biomass, and biofuels (Bond et al. 2004; 2007). Such particles in the atmosphere affect air quality (Lelieveld et al. 2001), impact human health (Dockery 2001; Jansen et al. 2005; Grahame and Schlesinger 2010), and have a significant effect on the direct and indirect radiative forcing of regional and global climate (Ramanathan and Carmichael 2008; Bauer et al. 2010). However, the detailed effects of black carbon particles on human health and climate remain highly uncertain (Seinfeld 2008). These uncertainties are magnified by the chemical and physical complexities of black carbon-containing particles (Adachi et al. 2010). Further, pollutant species co-emitted with black carbon by combustion sources can significantly influence the chemical composition and therefore key physical, chemical, and radiative properties of black carbon particles. A detailed, predictive understanding of the impacts of black carbon-containing particles on regional and global scales requires that the chemical composition and associated physical and optical properties of these particles can be quantified.

During the past decade, 2 different, real-time instrumental techniques have had direct and important contributions toward characterizing and quantifying carbonaceous particles' physical and chemical properties. The Single Particle Soot Photometer (SP2) developed by Droplet Measurement Technologies (DMT, Boulder, CO) is a real-time, highly sensitive, compact instrument that utilizes single particle incandescence signals to quantify refractory black carbon (rBC) mass loadings (Stephens et al. 2003; Baumgardner et al. 2004; Schwarz et al. 2006). The SP2 provides rBC mass loadings, particle number concentrations, and size distribution measurements, though these measurements are constrained by single particle detection limits of ~0.7 fg/particle (Schwarz et al. 2010). Several groups have combined the optical scattering and the incandescence signals to provide information on the internal mixing (i.e., coating) state

---

Received 23 September 2011; accepted 21 January 2012.

The authors acknowledge conceptual discussions with Darrel Baumgardner and are indebted to Chris Hare, Jason Olfert, Joel Kimmel, Donna Sueper, Hugh Coe, James Allan, Eben Cross, Sally Ng, David Liscinsky, Barry McManus, and Lino Gonzalez. The research was supported by DOE ASR #DE-FG02-05ER63995, DOE SBIR #DE-FG02-07ER84890, NSF ATM-0854916, NASA SBIR #NNX10CA32C, and NOAA Climate Program #NA09OAR4310125.

Address correspondence to T. B. Onasch, Aerodyne Research Inc., 45 Manning Road, Billerica, MA 01821, USA. E-mail: onasch@aerodyne.com

of measured rBC particles (Gao et al. 2007; Moteki and Kondo 2007; Shiraiwa et al. 2007; Schwarz, Gao, et al. 2008; Schwarz, Spackman, et al. 2008). However, the SP2 does not provide any chemical information.

The Aerosol Mass Spectrometer (AMS), developed by Aerodyne Research Inc., measures real-time, size-resolved composition of nonrefractory, submicron aerosol particle ensembles (Jimenez et al. 2003; Drewnick et al. 2005; Canagaratna et al. 2007). In the standard AMS configuration, aerosol particles are thermally vaporized at ∼600°C using a resistively heated, tungsten vaporizer. The resulting vapor is ionized with an electron beam and the ions are detected in a high-resolution mass spectrometer (DeCarlo et al. 2006). This method of vaporization precludes the detection of refractory aerosol components, including black carbon.

In this paper, we describe the development, validation, and initial application of a new instrument, designated the Soot Particle Aerosol Mass Spectrometer (SP-AMS), for characterizing and quantifying ambient rBC particles. The SP-AMS is a combination of the High Resolution Time-of-Flight Aerosol Mass Spectrometer (HR-ToF-AMS) and the Single Particle Soot Photometer (SP2); an intracavity Nd:YAG laser vaporizer (1064 nm), based on the design used in the SP2 instrument, has been incorporated into the HR-ToF-AMS. The new vaporizer is designed to vaporize refractory particle types that are not detected in a standard AMS and to provide vaporized species for detection via electron impact ionization for chemical ion generation, thereby keeping the vaporization and ionization steps separate. The addition of a laser vaporizer allows AMS technology to be directly applied, for the first time, to characterizing the refractory chemical components of ambient aerosol, specifically laser-light absorbing rBC particles. The new laser vaporizer does not interfere with the standard resistively heated vaporizer (referred to as the tungsten vaporizer from here on) used in an HR-ToF-AMS instrument or generate chemical ions. Therefore, the SP-AMS instrument can be operated with the laser vaporizer alone, with both the laser and tungsten vaporizers, or with the tungsten vaporizer alone.

## 2. INSTRUMENT DESIGN

The SP-AMS instrument is a standard HR-ToF-AMS with an added intracavity laser vaporizer. Figure 1 shows 2 schematic views of the SP-AMS highlighting the 3 axes of the instrument: particle beam, laser beam, and ion extraction into the mass spectrometer. The SP-AMS, like other AMS instruments, provides average mass spectrometric measurements of the ensemble of sampled aerosols rather than measurements on a particle-by-particle basis. This is in contrast to the SP2 instrument (Schwarz et al. 2010) and laser ablation aerosol mass spectrometers ((Murphy 2007; Pratt and Prather 2011) and references therein) that inherently provide single particle measurements. Furthermore, the laser vaporizer in the SP-AMS is a continuous wave (CW) laser with light power densities (i.e., irradiance) below multiphoton ionization and/or plasma formation thresholds, unlike single particle laser ablation instruments that rely on laser desorption and ionization techniques for ion generation (Murphy 2007). Thus, chemical ions in the SP-AMS and standard AMS instruments are generated using the universal 70 eV electron impact ionization technique. The addition of a laser vaporizer into the AMS design expands the utility of the AMS technology to include the detection of near-infrared light absorbing particles, specifically ambient rBC particles. The laser vaporizer has been designed as a module that can be added to any existing AMS instrument.

Data acquisition sampling modes of the SP-AMS are the same used in standard ToF-AMS instruments: Mass Spectrum (MS) and Particle Time-of-Flight (PTOF) modes (Jimenez et al. 2003; DeCarlo et al. 2006; Kimmel et al. 2011). The SP-AMS provides a difference measurement in MS mode, using a mechanical beam block to modulate the sampled particle beam for OPEN (sampled particles) and CLOSED (particle free) detection. An alternate sampling technique of the SP-AMS provides a similar measurement by turning the laser on and off, rather than using the mechanical chopper. In the PTOF mode, a mechanical chopper is used for measuring the mass distributions of both nonrefractory and refractory particulate material as a function of particle vacuum aerodynamic diameter ($d_{\mathrm{va}}$).

### 2.1. Laser Vaporizer

The incorporation of a laser vaporizer into an AMS includes several key challenges. The diode-pumped Nd:YAG intracavity laser has to efficiently couple the laser radiation into the AMS high vacuum ionization-detection chamber and overlap the particle beam. As illustrated in Figure 1, the laser cavity (crystal and coupling mirror) is located entirely within the AMS vacuum chamber to optimize laser performance. Thermal stability of the crystal is maintained by external thermo-electric cooling. Laser cavity alignment is provided by external mounts attached to the vacuum chamber, thereby providing stable beam alignment within the ionization-detection region in the SP-AMS. An externally mounted CCD camera is used for tracking the laser power, alignment, and the laser Transverse ElectroMagnetic (TEM) modes.

As shown in Figure 1, the SP-AMS has 3 orthogonal axes (particle beam, laser vaporizer, and ion extraction) and accurate alignment of the axes is important for reproducible and stable operation. Aerodyne AMS instruments utilize a cross-beam ion source (Pfeiffer Vacuum) and a tungsten filament (∼8 mm length wire) centered on the ion extraction axis and oriented along the particle beam axis. The standard tungsten vaporizer is set back from the ion extraction volume by ∼4 mm along the particle beam axis. The particle beam and laser vaporizer are aligned with respect to the tungsten vaporizer and intersect the ion extraction volume of the ion formation cage. Both vaporizers were designed such that vaporized molecules intersect the electron beam and the ion extraction volume; however, relative

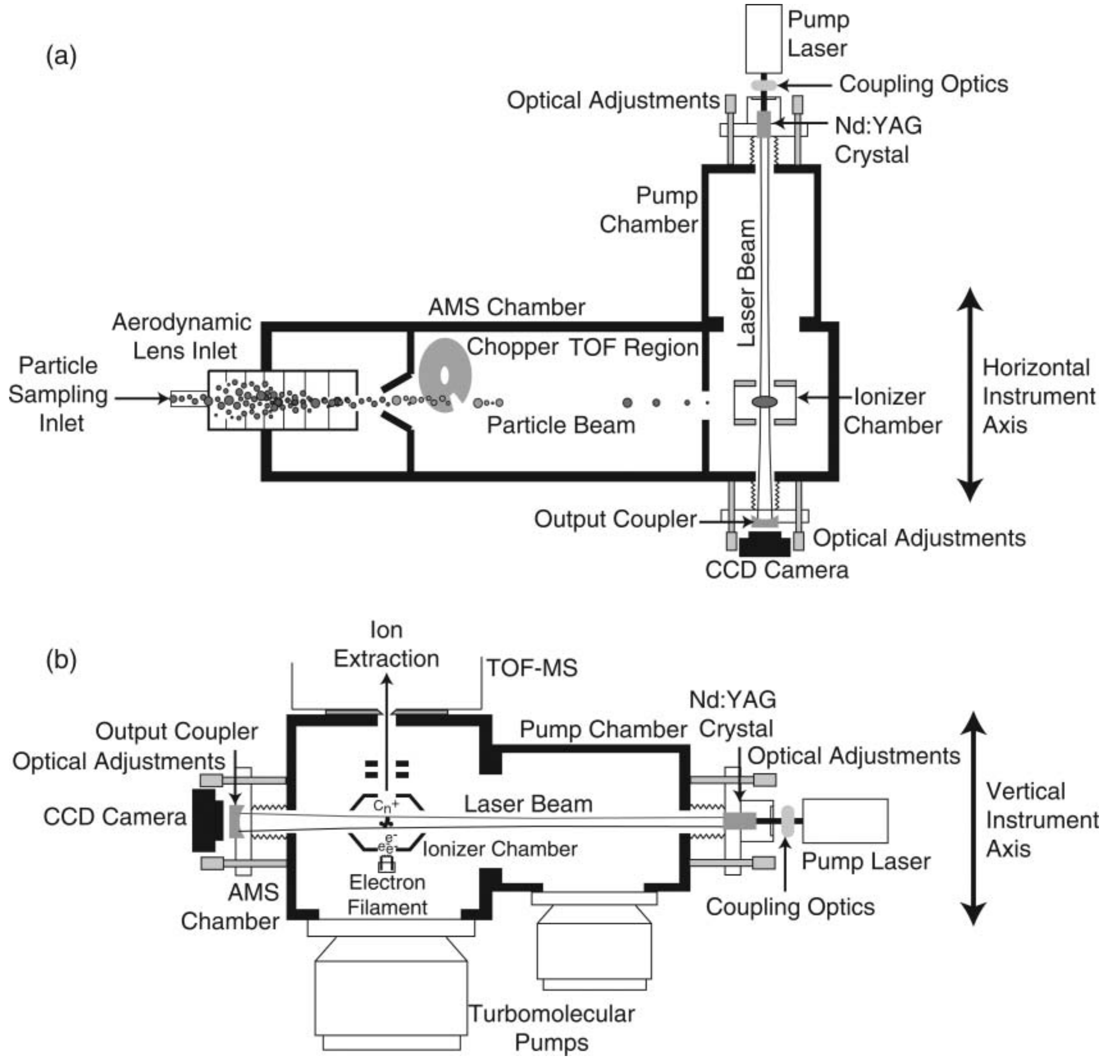

FIG. 1. Schematics of SP-AMS instrument that show the particle beam, laser beam, and ion extraction axes and define the horizontal and vertical axes of the instrument as discussed in the text. (a) Top-down view. (b) Cross-section view looking up the particle beam axis.

ionization efficiencies from the laser and tungsten vaporizers will depend upon the alignment and tuning of these elements.

It is important that the intensity of the laser light interacting with the absorbing particles be sufficient to fully vaporize particles as they cross the laser beam, but remain below multiphoton ionization and/or plasma formation thresholds. Thus, the ideal vaporizing laser configuration has a high intracavity power and a broad beam for sufficient particle–laser beam overlap. High intracavity laser power is required as particles sampled into the SP-AMS vacuum chamber ($\sim 1 \times 10^{-5}$ Torr) travel rapidly (~100 m/s) and spend little time (5–20 $\mu$s depending upon particle size) in the laser beam. In comparison, particles sampled into a SP2 instrument at atmospheric pressures travel through the laser beam in 30–600 $\mu$s, depending upon the sampling flow rate, which can be varied from approximately 0.25 to 4 $cm^3/s$ (Schwarz et al. 2006; Schwarz et al. 2010). Intracavity laser power has been optimized (intracavity laser power densities > 0.2 $MW/cm^2$) by using a free-beam pump laser configuration (808 nm, model JOLD-4.2-BAXH-1E, Jenoptik) and maximizing pump laser power. Current SP2 designs use a fiber coupled pump laser configuration and operate at lower pump laser powers (Schwarz et al. 2010). As described in Section 3.2.2, sufficient laser intensity can be checked by measuring the sensitivity of the SP-AMS to rBC particle carbon ion signals as a function of laser power.

The current SP-AMS utilizes the TEM00 laser mode (i.e., 2-D Gaussian profile). The laser beam width for the TEM00 mode is a function of the cavity length and limited by practical instrument dimensions to a relatively narrow width ($\sigma \sim 0.25$ mm, FWHM ~0.56 mm), which is similar to the laser beam width in SP2 instruments (Stephens et al. 2003). The width of the laser vaporizer is less than the average measured particle beam widths in AMS instruments for 5 of 6 field studies covering urban to rural environments (Salcedo et al. 2007). Further, it is significantly less than the estimated particle beam width (0.77 mm) for laboratory generated ethylene flame soot particles (Slowik et al. 2004; Huffman et al. 2005). Thus, dispersion of small and nonspherical particles in the aerodynamic lens inlet of the SP-AMS may cause particles to miss the laser TEM00 vaporizer. It is important to note that any mismatch in overlap between the particle and laser beams due to the narrow laser beam width occurs only along the vertical axis of the instrument (i.e., perpendicular to the plane defined by the particle and laser beams), the horizontal axis being the laser beam axis (Figure 1). This issue is investigated in more detail in Section 3.2.2. The use of higher-order modes is being explored as a potential way to broaden the laser beam vertically in the vaporization zone.

## 2.2. Vaporization and Detection

AMS technology provides a sensitive, linear response of chemical ions to sampled particle mass (Jayne et al. 2000; Takegawa et al. 2005). The technology is based on the separation of the vaporization of particulate material and the subsequent ionization of the vaporized species (Jayne et al. 2000). The AMS utilizes the universal 70 eV electron impact ionization technique, such that any chemical species that can be vaporized can be detected. The use of a resistively heated, tungsten vaporizer has precluded direct detection of refractory materials. The SP-AMS expands the application of this technology by using an intracavity, CW laser to vaporize rBC particles (and associated nonrefractory particulate species), which do not vaporize upon impact with a standard 600°C tungsten vaporizer. Figure 2 graphically displays the vaporization and detection processes within the SP-AMS laser vaporizer relative to the optical processes observed in SP2 instruments (Gao et al. 2007). From left to right in Figure 2, rBC-containing particles are aerodynamically focused into the laser beam under high vacuum. As the particles enter the laser beam, they begin to scatter laser light (top plot, red line). Once the absorbing material in the particles starts to heat up, nonrefractory material is vaporized from the particles decreasing the scattered light and generating neutral gas phase chemical species (bottom diagram). With the nonrefractory material vaporized from the particles, the rBC material heats up further to several thousand degrees K (Schwarz et al. 2006; Moteki and Kondo 2007; Moteki and Kondo 2010). The blackbody radiation at these elevated temperatures gives rise to the visible incandescence signal that is monitored in the SP2 instrument (top plot, blue line) while, simultaneously, the refractory portion of the particles vaporize into neutral carbon clusters (bottom diagram). In the SP-AMS, the vaporized species are subsequently ionized and detected by time of flight mass spectrometry (bottom diagram). Finally, it should be noted that particle heating and vaporization in the SP-AMS differs from that in the SP2 due to the high-vacuum environment where the particles cross the laser beam, such that small rBC particle detection in the SP-AMS is not limited due to convective cooling as it is in the SP2 (Schwarz et al. 2010).

Particle vaporization by absorbed CW laser light differs from particle flash vaporization upon impaction with a constant temperature tungsten surface (as is done in the standard AMS) in terms of collection efficiencies, internal energies of vaporized molecules, and maximum vaporization temperatures. The collection efficiency, *CE*, of an AMS is a product of 3 terms,

$$CE = E_{\mathrm{L}} \times E_{\mathrm{S}} \times E_{\mathrm{B}}, \qquad [1]$$

where $E_{\mathrm{L}}$ is the fraction of particles lost during transit through the inlet and aerodynamic lens, $E_{\mathrm{S}}$ is the fraction of particles lost due to particle beam divergence causing particles to miss the vaporizer (either laser or tungsten), and $E_{\mathrm{B}}$ is the fraction of particles lost due to particle bounce effects from the tungsten vaporizer prior to full vaporization (Huffman et al. 2005; Matthew et al. 2008). As noted above, the *CE* of the SP-AMS laser vaporizer is governed by the $E_{\mathrm{S}}$ term, whereas, the *CE* of the tungsten vaporizer is currently understood to be governed by the $E_{\mathrm{B}}$ term (Matthew et al. 2008).

As shown in Section 3.1, different mass spectral fragmentation patterns were observed for the same organic compound vaporized using the 2 different vaporizer techniques. As 70 eV electron impaction ionization is used for all SP-AMS measurements, the differences in the fragmentation are likely due to different internal energies of the vaporized organic compound (Vékey 1996; Wilson et al. 2006). These results suggest that the vaporization, and thus ionization, processes of neutral molecules vaporized from particles absorbing laser energy may not be the same as for particles impacting a heated tungsten surface in the SP-AMS. The characterization of particle material as refractory or nonrefractory is an operational definition connected to the detection capability of the instrument (DeCarlo et al. 2006; Schwarz et al. 2010). In the operation of the standard AMS, nonrefractory particle material (NR-PM) is defined as the particulate material that can be vaporized using a 600°C resistively heated vaporizer and detected during the instrument sampling interval (DeCarlo et al. 2006; Salcedo et al. 2010). Schwarz et al. (2010) defines rBC as the refractory carbon mass detected by incandescence signals in SP2 instruments. As the SP-AMS and SP2 instruments both use a similar 1064 nm CW laser to detect rBC particles, we adopt the Schwarz et al. (2010) definition for the rBC mass detected by the SP-AMS via aerosol mass spectrometry. In addition, for the fraction of particles that absorb SP-AMS laser light, the significantly higher maximum particle temperature attained by laser heating extends the range of detectable particle components up to rBC. This extended range includes the standard AMS nonrefractory mass (NR-PM) components as a subset. We designate the particle mass detected by the SP-AMS less the NR-PM and rBC components as refractory particulate matter (R-PM). R-PM may include refractory metals, inorganics, and organic species associated with rBC

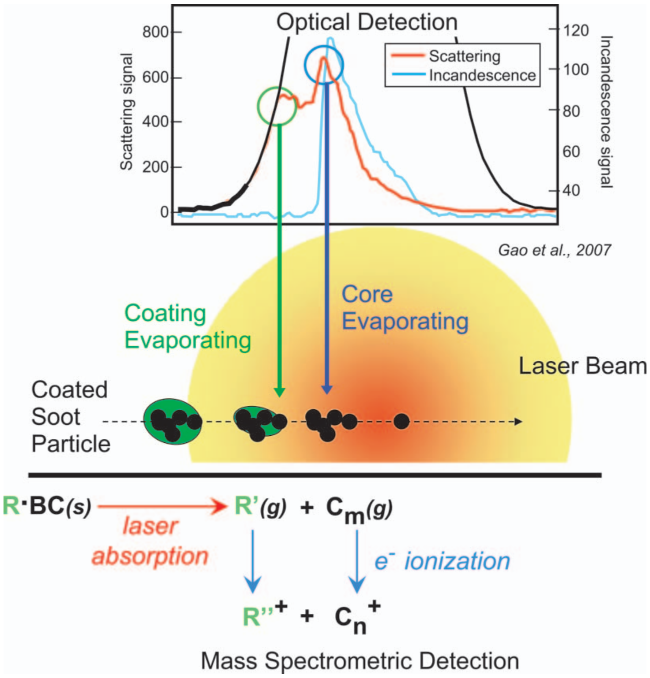

FIG. 2. Cartoon of coated soot particles passing through laser beam (from left to right), with transit times of 5–20 $\mu$s (dependent upon size). As the coated soot particle heats, the top plot shows measured light scattering (red) and incandescence signals (blue) as observed by an SP2 (Gao et al. 2007), and the bottom schematic shows the vaporization of nonrefractory species ($R'(g)$) and refractory carbon clusters ($C_m(g)$) and the resulting ions formed from electron impact ionization in the detection region of the SP-AMS. Subscripts s and g denote solid and gas phase, respectively.

particles. Table 1 summarizes the measured species and associated *CE* terms for the 3 vaporizer combinations of the SP-AMS.

The range of particle types that absorb 1064 nm wavelength light and are detected by either incandescence or mass spectrometry (i.e., any particulate material with a low enough electronic band gap) has been explored using SP2 instruments and include various rBC particles (e.g., graphitic, amorphous, fullerenic) as well as silicon, niobium, and chromium particles (Schwarz et al. 2006; Moteki and Kondo 2010). Recent work in our laboratory include detection of metal (e.g., aluminum, zinc, silver, and gold) and ceramic (e.g., boron carbide) nanoparticles suggesting this instrumental technique may have wide application in nanoparticle research. Here, we limit the focus of this paper to rBC particle detection for the specific application of characterizing and quantifying ambient rBC containing particles.

## 3. INSTRUMENT CHARACTERIZATION

### 3.1. Aerosol Mass Spectra and Interpretation

The fundamental measurement of the SP-AMS instrument is an average aerosol mass spectrum. In Figure 3, we show a SP-AMS generated mass spectrum of laboratory soot produced in the combustion of ethylene at a fuel equivalence ratio of 2 and thermally denuded at 250°C (Cross et al. 2010). The figure displays the measured ion count rate (Hz) as a function of the mass to charge ratio (m/z), with an inset highlighting signals above m/z 360 and a secondary inset highlighting signals around m/z 720. As the flame soot particles were denuded prior to sampling by the SP-AMS, the dominant ion signals in the

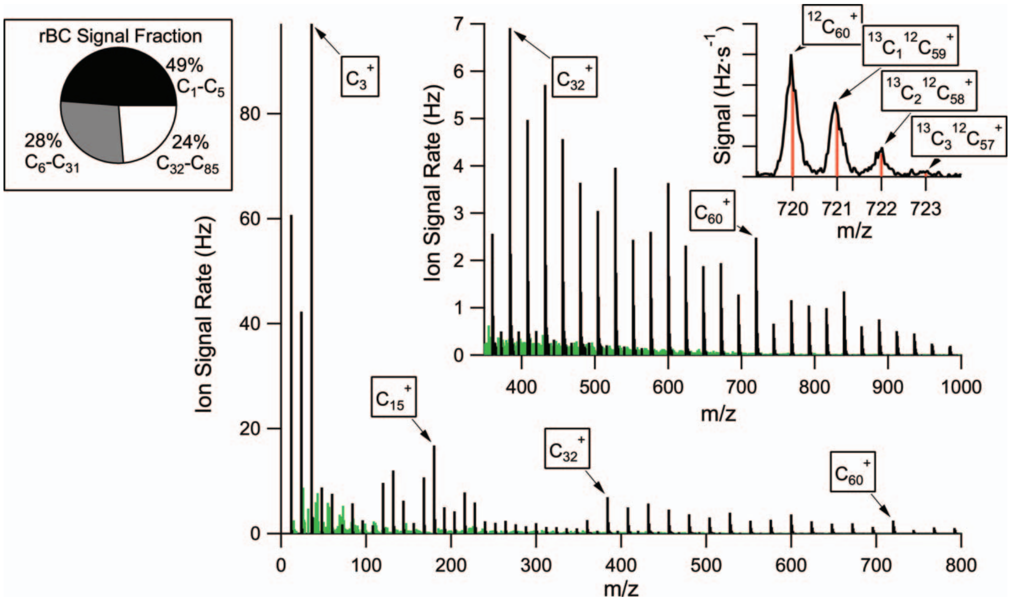

FIG. 3. Mass spectrum of denuded (250°C) ethylene flame soot averaged over 20 min. Carbon ion clusters are shown in black and organic signals (i.e., $C_xH_y$ and $C_xH_yO_z$) are shown in green. Significant carbon ion clusters are spaced 12 m/z apart (i.e., $C_1$) for m/z < 384 and 24 m/z apart (i.e., $C_2$) for m/z > 384. The first inset highlights the stable carbon ion cluster sequence for m/z greater than 384 (i.e., $C_{32}^+$), which are fullerene structures. The second inset shows the measured $^{13}C$ isotopic distribution (black; raw signal) compared with NIST values (red sticks) for the stable $C_{60}$ cluster, buckminsterfullerene. The pie chart shows the relative abundance of the carbon ion clusters for $C_1$–$C_5$ (49%), $C_6$–$C_{31}$ (28%), and $C_{32}$–$C_{85}$ (24%).

TABLE 1
SP-AMS measured particulate species for the 3 vaporizer combinations

| Vaporizer | Measured species |
|---|---|
| Tungsten | NR-PM * $E_B$ |
| Laser | (rBC + R-PM$^‡$ + NR-PM$^‡$) * $E_S$ |
| Laser and tungsten | (rBC + R-PM$^‡$ + NR-PM$^‡$) * $E_S$ + (NR-PM - NR-PM$^‡$ * $E_S$) * $E_B$ |

NR-PM = Nonrefractory Particulate Material measured by a standard AMS (Jimenez et al. 2003)
R-PM = Refractory Particulate Material measured by the SP-AMS (see text for details)
rBC = Refractory Black Carbon measured by the SP-AMS and SP2 (Schwarz et al. 2006)
$^‡$ = Particulate Material on rBC particles as measured by the SP-AMS (see text for details)
$E_B$ = Particle bounce related Collection Efficiency of the AMS
$E_S$ = Size and shape related Collection Efficiency of the SP-AMS

mass spectrum are derived from refractory particulate material. Using high-resolution mass analysis, all of the peaks shown in black are identified as carbon ions from $C_1^+$ (m/z = 12) up to $C_{82}^+$ (m/z = 984), shown in the first inset. These rBC ion signals are not observed using standard AMS instruments with tungsten vaporizers (Slowik et al. 2004; Cross et al. 2010). The sum of these carbon ions is a measure of sampled particulate refractory carbon mass and the distribution of the ion signals across the various carbon ions provides a "finger print" for ethylene flame soot. Such "finger prints" may be influenced by the laser vaporization process as observed for pulsed laser vaporization and ionization experiments (Spencer et al. 2008). The "finger prints," even if modified by the laser vaporization process, may be related to the molecular structure of carbon in soot particles and may provide useful information for apportioning mass loading of ambient rBC particles to different combustion sources.

A large fraction of the summed carbon ion signal (∼50%) resides in the $C_1^+$ to $C_5^+$ ion signals, with the largest carbon ion signal at $C_3^+$. The intensities of these peaks exhibit a pattern with clusters of odd numbers of carbons being larger (i.e., more stable) than clusters with even number of carbons as previously observed (Drowart et al. 1959). The mass spacing for the dominant rBC ion signals below $C_{30}^+$ is m/z = 12 (i.e., a single carbon atom), whereas the spacing for dominant carbon ion signals above $C_{30}^+$ is m/z = 24 (i.e., 2 carbon atoms). This change in spacing represents a change from carbon clusters with open 2-D structures (e.g., linear chains, monocyclic rings, and polycyclic rings) to closed or hollow 3-D, stable fullerene structures (Bloomfield et al. 1985; von Helden et al. 1993). The first component in this spectral region may have either thirty or thirty-two carbon atoms, in agreement with previous studies indicating that $C_{30}$ or $C_{32}$ may be the smallest stable fullerene structure (von Helden et al. 1993; Kietzmann et al. 1998). Several large, stable fullerenes, including $C_{60}^+$ at m/z 720 (i.e., buckminsterfullerene) also stand out in the sequence. The second inset in Figure 3 shows an expansion around m/z 720 in which the $^{13}$C containing isotopes of $C_{60}^+$ are clearly present in the raw mass spectrum and comparison with NIST isotope distribution (red sticks) confirms the identification. Integrated SP-AMS rBC signals presented and discussed in this paper include all measured carbon ions from $C_1^+$ to at least $C_{60}^+$. The maximum m/z range sampled, and thus the maximum carbon ion cluster, varied slightly between experiments.

In addition to measuring rBC ion signals, the SP-AMS also provides mass spectral information on the nonrefractory components. The minor, more complex part of the denuded soot spectrum shown in green in Figure 3 are organic ions, identified as $C_xH_y$ and $C_xH_yO_z$ mass fragments, from organic components on the soot particles that remain after passage through the denuder. The mass spectral information of nonrefractory components are further illustrated by comparing mass spectra obtained in a SP-AMS with the laser vaporizer turned on and off while the standard tungsten vaporizer remains on. In Figure 4a, the mass spectrum of nascent (i.e., not denuded) soot particles, generated using a propane diffusion flame source (different soot source than used to obtain data in Figure 3), is measured under 2 conditions: (i) laser-on and vaporizer-on (top panel), and (ii) laser-off and vaporizer-on (middle panel). The difference between the laser-on and laser-off spectra is shown in the bottom panel. In the laser-on experiment, ion signals associated with both the nonrefractory organics and rBC are present. With the laser off, only the mass spectrum associated with nonrefractory organics is observed.

The largest mass components in the difference spectrum (bottom panel of Figure 4a) are the rBC ion signals (black) and an ion signal at m/z = 44, associated with $CO_2^+$ (violet). Other smaller ion signals, associated with $C_xH_y$ and $C_xH_yO_z$ fragments, are also present in the difference spectrum.

The data shown in Figure 4a are displayed in a different form in Figure 4b. Here, we show the sum of the ion signals (Hz) associated with the nonrefractory organics, rBC, and $CO_2^+$ components, for the 2 different configurations: laser-on, and laser-off. The $CO_2^+$ signal in Figure 4b includes additional signal attributed to $CO_2^+$ ion formation described in fragmentation table entries and discussed elsewhere (Allan et al. 2004; Aiken et al. 2007). As is evident, with the laser on, the rBC signal, the $CO_2^+$ signal, and the organic signal are all present. With the laser off, the organic signal remains although it decreases by about 20%. The rBC and the $CO_2^+$ signals disappear.

The $CO_2^+$ signal that disappears in the laser-off experiment is not observed in 2 other different types of rBC particles (i.e., the denuded soot shown in Figure 3 or in the mass spectrum of glassy carbon spheres, not shown). Therefore, we conclude that this signal observed in the Figure 4 mass spectrum originates from the particle composition rather than from products of laser induced oxidation of carbon. Tentatively, we suggest that the source of this signal is refractory oxygenated soot compounds.

The observed 20% decrease in the nonrefractory organics from the laser-on to laser-off conditions may be due to several factors. First, there may be oxygenated organics present that are more refractory (i.e., lower vapor pressure) than can be thermally vaporized by the tungsten vaporizer. Second, particle bounce from the tungsten vaporizer may reduce the laser-off collection efficiency (i.e., $E_B < 1$). Third, particles vaporized by the laser generate vapor plumes at the intersection of the electron beam and the ion extraction axis of the mass spectrometer with efficient detection, whereas particles vaporized by the tungsten vaporizer are generated beyond the ion extraction axis with potentially lower detection efficiency. This issue is the focus of on-going studies.

Additional information is often necessary for the proper identification of the SP-AMS mass spectra. For $m/z = 24$ ($C_2^+$) and greater, the rBC ion signals are present only with the laser on, as is evident in Figure 4a. However, a fraction of the $C_1^+$ signal at $m/z = 12$ is present also with the laser-off (i.e., tungsten vaporizer only), albeit small in Figure 4a. Therefore, the laser-off fraction (i.e., nonrefractory organic contribution) of the $C_1^+$ signal must be subtracted from the summed carbon ion signals to obtain a quantitative measure of the rBC. We suggest apportioning the rBC fraction of the $C_1^+$ signal based on the $C_3^+$ signal, as the $C_3^+$ signal is the largest rBC ion signal, is not detected using tungsten vaporizer only, and is unambiguously identifiable with a high-resolution mass spectrometer (i.e., HR-ToF-AMS; $M/\Delta M \sim 1000$).

The capability of the SP-AMS to identify nonrefractory organic components associated with laser-light absorbing rBC particles is similar to standard AMS instruments, though the fragmentation patterns observed in average mass spectra of the nonrefractory components may differ. As shown and discussed in Section 1 of the online Supplemental Information (SI), SP-AMS-generated nonrefractory mass spectra of the compound dioctyl sebecate (DOS; CAS 122-62-3; molecular weight = 426.5 g/mol), vaporized using the laser vaporizer from coated rBC particles, exhibit less fragmentation than for pure DOS particles vaporized using the tungsten vaporizer. As discussed in Section 2.2, less fragmentation likely implies a lower internal energy imparted to the DOS during vaporization from the laser-heated particles than imparted by the 600°C tungsten vaporizer, although the final temperature attained by the refractory portion of the particles is considerably higher. This result is consistent with the schematic in Figure 2, which shows that the temperature at which the coating vaporizes is less than the temperature at which the refractory carbon vaporizes. These results suggest that SP-AMS nonrefractory organic mass spectral signals can be analyzed with methods, such as Positive Matrix Factorization (PMF; Paatero and Tapper 1994; Ulbrich et al. 2009), to provide chemical information similar to that obtained by a standard AMS instrument, but may differ slightly in the fragmentation patterns.

The SP-AMS also measures the ion signal (and mass) distributions as a function of particle size as is illustrated in Figure 5. This figure shows ion signal distributions as a function of vacuum aerodynamic diameter ($d_{va}$) for atomized and mobility size-selected (225 nm) conglomerate particles consisting of 50 nm glassy carbon spheres coated via gas-to-particle deposition with varying thicknesses of DOS. Figures 5a–c show glassy carbon spheres uncoated and coated with 4 nm and 8 nm layers of DOS, respectively. The coating thickness estimates were obtained using simultaneous mobility diameter measurements (not shown). As is evident, uncoated glassy carbon spheres contain only rBC ion signals. Coated particles contain both rBC (black) and organic (green) components. The integrated rBC ion signal remains the same, independent of the coating. The organic signal (magnitude displayed on the right hand axis) increases with coating thickness, while the shape factor of the conglomerate glassy carbon sphere particles decreases to a limit of unity for spheres and the density of the particles decreases to the organic density. The measured increase in the $d_{va}$ of the coated distributions is dominated by the decreasing shape factor (refer to Section 2 in SI).

The monodisperse distribution mode, as best illustrated from the rBC ion signal, shifts to larger diameters with coating as expected. Additional information is obtained from the displacement toward higher $d_{va}$ of the organic ion signal distribution relative to the rBC ion signal distribution for the coated particles. This suggests that the particles in the glassy carbon sphere ensemble are not coated evenly. Some of the particles remain uncoated or only lightly coated. These particles retain a lower $d_{va}$ compared to the more fully coated particles and their associated black carbon signal does not fully coincide with the organic signal. This effect increases the width and decreases the height of the rBC distributions with coating.

## 3.2. Instrument Calibration and Sensitivity

In this section, we present a protocol for calibrating the measured ion count rates provided by the SP-AMS operated with a laser vaporizer to quantify both refractory and nonrefractory components of sampled particles containing rBC.

### 3.2.1. *Formulation of mass calibration*

As detailed in previous publications (Jimenez et al. 2003; Allan et al. 2004), the mass concentration of a specific chemical species $s$ ($\mu g/m^3$) can be derived from AMS measurements of

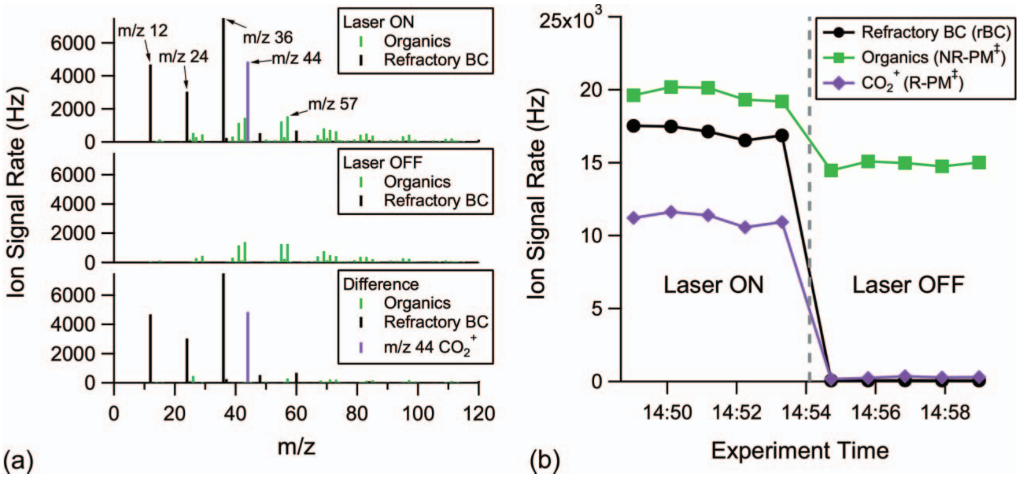

FIG. 4. Laboratory generated nascent soot sampled by a SP-AMS with both laser and tungsten vaporizers. The mass spectra in (a) show the laser-on, laser-off, and the difference (laser-on – laser-off) conditions. Carbon ions are shown in black, organic ions in green, and $CO_2^+$ ion signal is highlighted in violet in the difference spectrum. The integrated ion signals for refractory carbon, organic, and $CO_2^+$ (including fragmentation table entries derived from $CO_2^+$ ion signals) are shown in (b) as a function of experiment time.

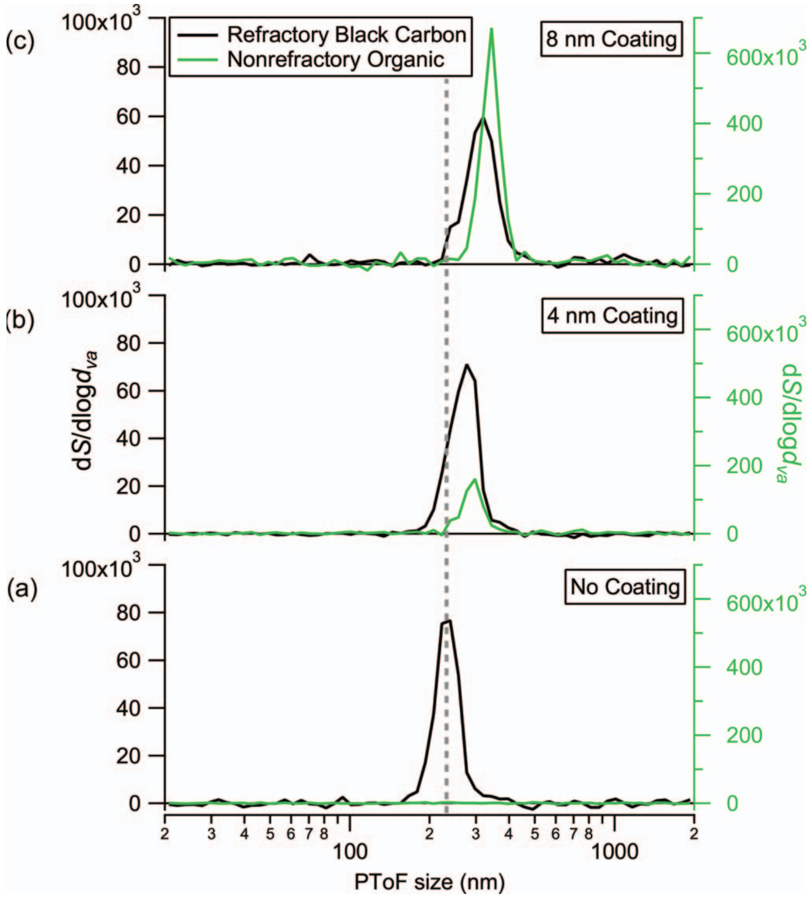

FIG. 5. Size distributions for uncoated (a) and DOS oil coated (b and c) monodisperse 225 nm particles generated by atomizing and size selecting 50 nm glassy carbon spheres from a water suspension. The carbon ion signals (black) are plotted on the left axes and the organic ion signals (green) are plotted on the right axes, both normalized to the $\log_{10}$ size bin width (i.e., $dS/d\log d_{va}$). The vertical line through the mode of the uncoated particle distribution is to emphasize shift in $d_{va}$ with added DOS. The coating thickness estimates come from measured mobility diameters.

the summed ion rate, $I_s$ (Hz = ions/s), by,

$$C_s = 10^{12} \frac{MW_{NO_3}}{RIE_s \cdot IE_{NO_3} \cdot Q \cdot N_A} \sum_i I_{s,i}, \quad [2]$$

where the factor $10^{12}$ is used for unit conversions, $MW_{NO3}$ is the molecular weight of nitrate (62 g/mol), $N_A$ is Avogadro's number (6.022 × $10^{23}$ molecules/mole), $Q$ is the sample flow rate (typically 1.4 $cm^3/s$), $IE_{NO3}$ is the ionization efficiency for nitrate (ions measured per molecules of nitrate sampled), and $RIE_s$ is the relative ionization efficiency of species $s$ to nitrate, defined as the ratio $(IE_s/MW_s)/(IE_{NO_3}/MW_{NO_3})$.

Here, we note that Equation (2), and thus the interpretation of AMS calibrations in general, can be simplified by changing to mass specific ionization efficiencies (i.e., ions detected per particulate mass sampled for a given species) with the particulate mass in units of picograms (i.e., $10^{-12}$ grams). The mass specific ionization efficiency for nitrate, $mIE_{NO_3}$, in units of ions/picogram is equal to:

$$mIE_{NO_3} = \frac{10^{-12} \cdot IE_{NO_3} \cdot N_A}{MW_{NO_3}}. \quad [3]$$

Substituting the mass specific ionization efficiency of nitrate (Equation (3)) into Equation (1), the mass concentration of a specific chemical species $s$ ($\mu g/m^3$) is simply:

$$C_s = \frac{\sum_i I_{s,i}}{RIE_s \cdot mIE_{NO_3} \cdot Q}, \quad [4]$$

where,

$$RIE_s = \frac{mIE_s}{mIE_{NO_3}}. \quad [5]$$

$RIE_s$ is now defined as the ratio of the mass specific ionization efficiencies ($mIE_s/mIE_{NO_3}$), which is the same as previously defined though without requiring an explicit $MW_s$ value.

A calibration of the SP-AMS for refractory or nonrefractory particulate material, $s$, as shown in Equations (4) and (5), requires the measurement of at least 2 of the 3 variables: $RIE_s$, $mIE_s$, and $mIE_{NO_3}$. Here, we measure the mass specific rBC ionization efficiency, $mIE_{rBC}$, and the relative ionization efficiency of rBC, $RIE_{rBC}$.

### *3.2.2. Mass calibration for refractory black carbon particulate mass*

The rBC calibration (i.e., $mIE_{rBC}$) has been obtained using monodisperse rBC particles characterized with a Condensation Particle Counter (CPC; TSI model 3022a) to measure particle number concentrations and a Couette Centrifugal Particle Mass Analyzer (CPMA) that provides a shape-independent measure of per particle mass using centrifugal and electrostatic forces (Olfert and Collings 2005; Olfert et al. 2006).

Measurements were performed with 3 types of size-selected particles: atomized Regal black (REGAL 400R pigment black, Cabot Corp.), nascent ethylene flame soot, and denuded (250°C) ethylene flame soot. These measurements were performed as part of a soot particle instrument inter-comparison study, and the experimental details of particle generation and instrument measurements obtained have been published elsewhere (Cross et al. 2010). The atomized Regal black particles were highly compact in shape, as characterized by a mass-mobility exponent of ∼3. For Regal black, the particle mobility diameters ranged from 100 nm to 300 nm and exhibited an effective density (calculated from the ratio of the CPMA measured particle mass to mobility diameter derived particle volume) that changed with selected mobility diameters. The measured effective densities are provided in Section 3 of the SI and are similar to the effective densities measured for other black carbon particle types (Gysel et al. 2011). The ethylene flame soot particles were nonspherical, exhibiting a CPMA measured mass-mobility exponent of ∼2.2 for nascent soot and ∼2.1 for denuded soot (Cross et al. 2010). For nascent and denuded soot particles, the particle mobility diameters ranged from 100 nm to 300 nm.

Figure 6a shows the SP-AMS summed rBC ion signals normalized to the particle number concentration plotted as a function of CPMA measured per-particle black carbon mass. The CPMA black carbon mass for atomized Regal black and denuded soot particles is plotted as measured. The CPMA measured per-particle black carbon mass for nascent soot particles is obtained from denuded measurements of the nascent soot, which, as shown in Cross et al. (2010), is approximately 74% of the nascent soot particle total mass. The calibration for atomized Regal black particles yields $mIE_{rBC} = 140 \pm 6$ ions/pg. As stated previously, the SP-AMS ion signals are dependent upon the ion optics tuning and laser–particle beam overlap. Subsequent rBC calibrations, conducted using a variety of independent black carbon mass measurements (e.g., SP2 and MAAP) or relying on the CPMA-SMPS measured effective density given above, indicate instrument sensitivities ranging from the current calibration of 140 to 300 ions/pg of rBC.

As is evident in Figure 6a, the SP-AMS rBC calibration appears to depend on the particle type. For nascent ethylene flame soot, the calibration is 24 ± 10% lower (i.e., CE ∼ 0.75) and for denuded soot it is 60 ± 10% lower (i.e., CE ∼ 0.4) than the Regal black calibration. The likely reason for the lower refractory carbon signal observed in Figure 6a for ethylene flame soot particles is due to incomplete overlap between the particle and laser beams. The size range studied during this experiment was too narrow to provide useful information on any potential size-dependent CE trends. Supporting evidence for this conclusion includes a positive correlation between the measured $mIE_{rBC}$ (Regal black > nascent >

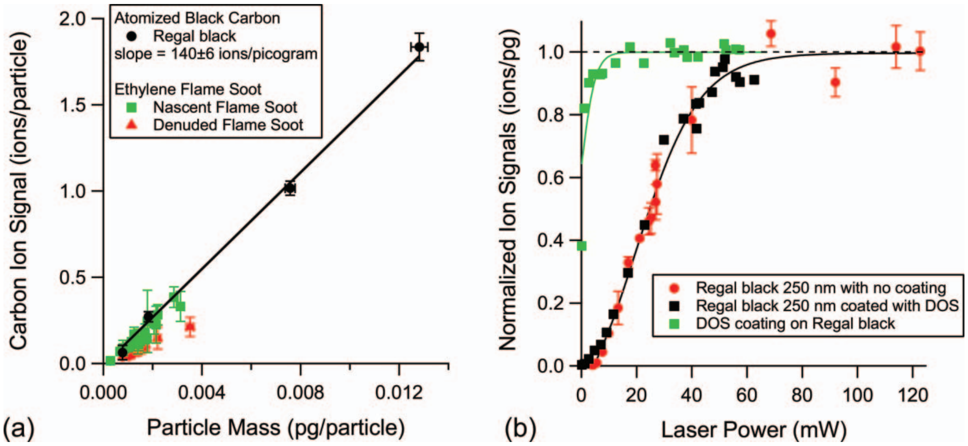

FIG. 6. SP-AMS rBC calibration. (a) SP-AMS integrated carbon ion signals per particle versus the per particle mass as measured by a CPMA for atomized Regal black and nascent and denuded (250°C) ethylene flame soot particles. The change in slope (Regal black < nascent < denuded) is related to collection efficiency differences caused by greater particle beam divergence for nonspherical particles. See text for details. (b) Normalized sensitivity curve for the SP-AMS (carbon ion signal per rBC particle mass) for uncoated (red) and DOS coated (black) 250 nm Regal black particles as a function of the laser power measured passing through the output coupler mirror. The normalized DOS organic ion signal per particle mass for the coated particles (green) saturates at lower laser power than the refractory carbon ion signals as expected due to the less refractory nature of DOS.

denuded) and measured mass-mobility exponents ($\sim 3 > 2.2 > 2.1$) and effective densities ($\sim 1.4 > 0.6 > 0.5$) derived from the ratio of the vacuum aerodynamic to mobility diameters. To address this issue, we are systematically implementing a particle beam width probe (Huffman et al. 2005) and investigating methods for broadening the laser beam while maintaining sufficient intensity.

Figure 6b displays the relative rBC ion signal as a function of vaporizing laser power (measured behind the output coupler) obtained with the SP-AMS for Regal black particles with mobility diameters of $d_m = 250$ nm. Included in the figure are atomized Regal black particles with and without DOS coatings. Independent of coating, the rBC ion signals reach a plateau at higher laser powers indicating that rBC detection is not limited by laser power or affected by DOS coatings. Measured beam widths ($\sigma$) for size-selected Regal black particles without any coatings are ~0.4 mm, which is similar in width to size-selected ammonium nitrate and PSL particles (Huffman et al. 2005), but still narrower than the laser beam width (Section 2.1). Thus, these black carbon particles exhibit the narrowest particle beams we can currently generate and minimize particle–laser beam overlap issues. Therefore, calibrating the SP-AMS using atomized Regal black particles is our recommended standard calibration for rBC.

The relative organic ion signals shown in Figure 6b obtained for the SP-AMS for the DOS coatings exhibit a similar behavior with laser power to the rBC signals, but attain saturation at lower laser powers. This result is expected as the DOS coatings vaporize at significantly lower particle temperatures than the rBC, as shown in the schematic in Figure 2. These results underscore the importance of operating with sufficient light intensity to fully vaporize rBC containing particles during transit through the laser as well as maximizing laser beam and particle beam overlap.

### 3.2.3. *Measurement of the relative ionization efficiency of refractory black carbon ($RIE_{rBC}$)*

$RIE_{rBC}$ was measured via independent measurements of $mIE_{rBC}$ and $mIE_{NO3}$ using the same SP-AMS instrument with

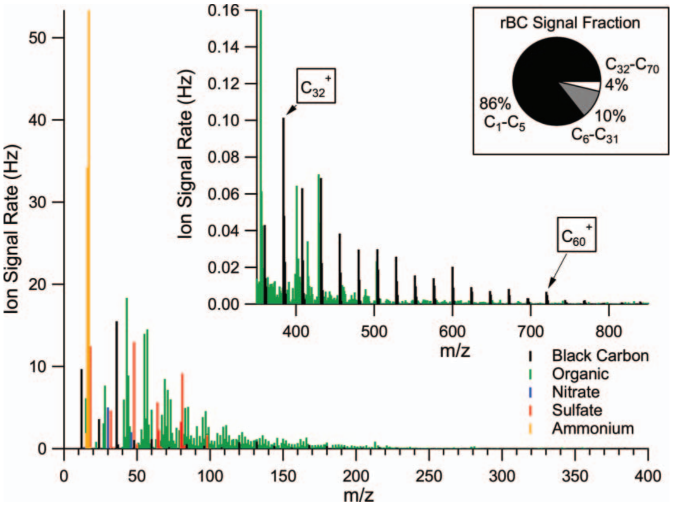

FIG. 7. Average mass spectrum (Hz) for ambient data sampled using a SP-AMS (laser vaporizer only) from a busy urban street in Chestnut Hill, MA. The figure shows the relative ion signals for rBC (black) and the nonrefractory chemical species, organics (green), sulfates (red), nitrates (blue), and ammonium (orange), on the black carbon particles. The first inset shows the measured fullerene ion series observed in ambient data. The pie chart shows the relative abundance of the carbon ion clusters for $C_1$–$C_5$ (86%), $C_6$–$C_{31}$ (10%), and $C_{32}$–$C_{70}$ (4%).

laser and tungsten vaporizers, respectively, and calculated using Equation (5). Seven independent pairs of $mIE_{\mathrm{rBC}}$ and $mIE_{\mathrm{NO3}}$ calibrations were conducted on the same SP-AMS over a period of a few weeks. The particles were generated by atomization of a solution (suspension) of the ammonium nitrate (Regal black), dried via a diffusion drier to relative humidities less than ∼30%, and size selected (250 nm) by a Differential Mobility Analyzer (DMA; TSI model 3080). In each experiment, the mass of doubly charged particles was less than 10% of the total. The average $mIE_{\mathrm{rBC}}$ measurement was 220 ± 40 ions/pg (instrument tuning was different than for calibrations shown in Figure 6a) and the average $mIE_{\mathrm{NO3}}$ measurement was 1200 ± 120 ions/pg. The resulting $RIE_{\mathrm{rBC}} = 0.2 \pm 0.1$ (2 $\sigma$ uncertainty). Thus, rBC is measured with a sensitivity ∼5 times lower in the SP-AMS than particulate nitrate.

To verify that the $RIE_{\mathrm{rBC}}$ value obtained using independent vaporizers in the same SP-AMS is appropriate for quantifying nonrefractory particulate material on rBC particles ($NR\text{-}PM^{\ddagger}$; refer to Table 1), we used the $mIE_{\mathrm{rBC}}$ obtained from Figure 6a and the measured $RIE_{\mathrm{rBC}}$ to quantify DOS coating material on laboratory generated ethylene flame soot particles. Figure S2 shows the comparison of the calibrated SP-AMS organic mass per particle (obtained using particle number concentration measurements by a CPC) on soot particles to the measured per particle DOS mass obtained by CPMA measurements. The CPMA measurements were obtained by the difference in the total per particle mass measurements for DOS coated soot particles and the refractory component after thermally denuding (250°C) the organic coating. These particles were 170 nm mobility size-selected soot particles (∼1.3 fg/particle; mass-mobility exponent of ∼2) coated with DOS to beyond ∼30 fg/particle (Cross et al. 2010). The best-fit line, assuming independent variables with errors, has a slope of 1.1 ± 0.1. This result suggests that the measured $RIE_{\mathrm{rBC}}$ is appropriate for quantifying the nonrefractory particulate material on rBC particles. More work is needed to verify the universality of this result.

### 3.2.4. *Sensitivity*

The sensitivity (or detection limit) of the SP-AMS instrument is described in terms of an Allan standard deviation plot shown in Figure S3. The Allan plot shows the noise level (standard deviation, $\sigma$) of measured carbon ion signals converted to rBC mass loadings ($\mu$g/m$^3$) for filtered (i.e., particle free) air as a function of increasing integration time, compared with white noise that decreases with the square root of the number of samples. The standard deviation of rBC as measured by the SP-AMS decreases as the square root of integration time up to about 200 s. Beyond that point, longer averaging times do not improve the signal-to-noise due to baseline drift. The 3$\sigma$ detection limits for rBC mass concentration measurements are 0.26 $\mu$g·m$^{-3}$ for 1 s sampling and 0.03 $\mu$g·m$^{-3}$ for 1 min collection. The organic and sulfate detection limits are 1.8 times higher and 0.2 times lower, respectively, in line with previously published results for HR-AMS instruments (DeCarlo et al. 2006).

## 3.3. Ambient Measurements

A SP-AMS with only a laser vaporizer was used to demonstrate the application of this new technique for ambient measurements. The SP-AMS was used to characterize ambient rBC-containing particles sampled through a window in the Boston College laboratory over a spring weekend. The laboratory overlooks a busy, urban street in Chestnut Hill, MA. The average particulate mass spectrum for rBC particles over the total sampling period is shown in Figure 7. The rBC ion signals are shown in black, with the fullerenes highlighted in the inset. The mass spectrum in this figure is analogous to the mass spectrum for laboratory soot shown in Figure 3. However, the spectrum here is dominated by nonrefractory organic and inorganic signals. Furthermore, the rBC ion distribution (shown in the pie charts in Figures 3 and 10) of the ambient data is dominated by the small carbon cluster ions ($C_1$–$C_5$), whereas the laboratory generated soot exhibits significantly more rBC ion signals for larger carbon ions ($>C_6$). The difference in measured rBC ion distributions may be due to different soot particle formation mechanisms (e.g., diffusion flame versus diesel engines). The ability of the SP-AMS to detect and identify various rBC ions, and nonrefractory (NR-PM$^{\ddagger}$) and refractory (R-PM$^{\ddagger}$) chemical species associated with the rBC particles, may serve as a means for source apportionment of rBC particles.

In addition to the SP-AMS, a calibrated MAAP instrument measured black carbon mass loadings via optical absorption. Figure 8a shows the SP-AMS (black) and the MAAP (red) measured black carbon mass loadings as a function of time for 3 min averages. As is evident, the agreement between the black carbon measurements is good ($R^2 = 0.76$), including during the sharp spikes in black carbon concentrations. For this data set, the SP-AMS was calibrated using the MAAP rBC measurements, such that the absolute SP-AMS sensitivity ($mIE_{\mathrm{rBC}}$) and collection efficiency ($CE$) were not independently quantified.

Figures 8b and c show the NR-PM$^{\ddagger}$ and R-PM$^{\ddagger}$ components (organics, sulfates, nitrates, ammonium, chloride, and iron) associated with the rBC-containing particles. The inorganic and metals signals do not appear well correlated with the magnitude of rBC, at least with respect to the obvious rBC plumes, suggesting that these species became associated with the rBC particles through secondary (i.e., gas-to-particle deposition or coagulation) mechanisms rather than being components of primary emissions. Through most of the sampling period, the NR-PM$^{\ddagger}$ organic loading (green) measured by the SP-AMS correlate with the rBC loadings, including for most of the rBC plumes. However, there are distinct periods when the chemical composition of the measured rBC particles changed significantly, with some plumes dominated by black carbon and some by organic material. Two such plumes with differing rBC and organic

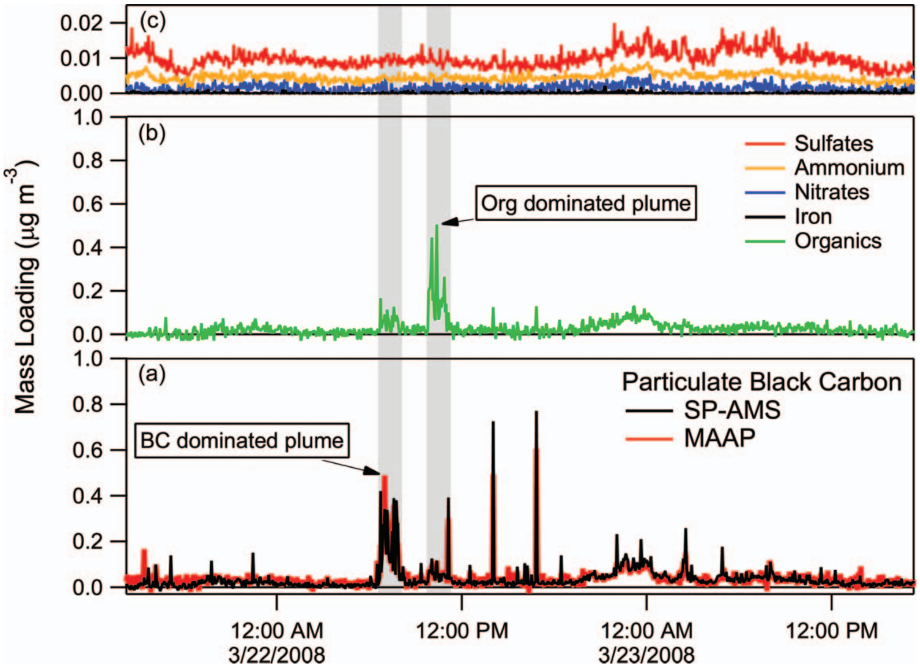

FIG. 8. Time dependent ambient data obtained with the SP-AMS (laser vaporizer only) and a MAAP black carbon absorption instrument in Chestnut Hill, MA. The SP-AMS and MAAP black carbon measurements (a) are correlated ($R^2 = 0.76$) and show multiple aerosol plumes containing black carbon particles. The SP-AMS nonrefractory organic (b) and inorganic (c) particulate mass associated with rBC particles are shown to be dominated by organic species. Two broad plumes (~1.5 h) are highlighted; one plume is dominated by black carbon mass and the other by nonrefractory organic mass.

compositions and lasting ~1.5 h each are highlighted in the figure as "rBC dominated" and "Org dominated."

The organic mass spectra for these 2 plumes (not shown) are similar to each other ($R^2 = 0.86$), both exhibit a high H:C ratio of ~1.9 and a low O:C ratio of ~0.1, and both are dominated by the hydrocarbon ion series for saturated alkyl compounds ($C_nH_{2n+1}$), slightly unsaturated alkyl compounds such as alkenes or cycloalkanes ($C_nH_{2n-1}$), and unsaturated alkyl compounds such as alkynes, dienes, and cycloalkenes ($C_nH_{2n-3}$; McLafferty and Turecek 1993). Furthermore, both the spectra appear similar to previously published diesel exhaust and lubrication oil spectra (Canagaratna et al. 2004), though the organic SP-AMS spectra obtained here exhibit reduced fragmentation, similar to trend illustrated in Figure S1. Thus, the organic components for these 2 plumes are hydrocarbon-like organic aerosol (HOA).

Figure 9 shows PToF-measured particle $d_{\mathrm{va}}$ size distributions associated with (a) the "rBC dominated" plume shown in Figure 8 and (b) the "Org dominated" plume. The rBC mass loading in the "rBC dominated" plume peaks at $d_{\mathrm{va}} \sim 120$ nm, which is similar in size to diesel exhaust particulate emissions measured using a standard AMS ($d_{\mathrm{va}} \sim 90$ nm; Canagaratna et al. 2004), aircraft exhaust particulate emissions ($d_{\mathrm{va}} \sim 100$ nm; Onasch et al. 2009), and laboratory generated propane and ethylene flame soot ($d_{\mathrm{va}} \sim 100$ nm; Slowik et al. 2004; Cross et al. 2010). These similarities potentially link the "rBC dominated" plume with fresh emissions of nonspherical (i.e., fractal-like)

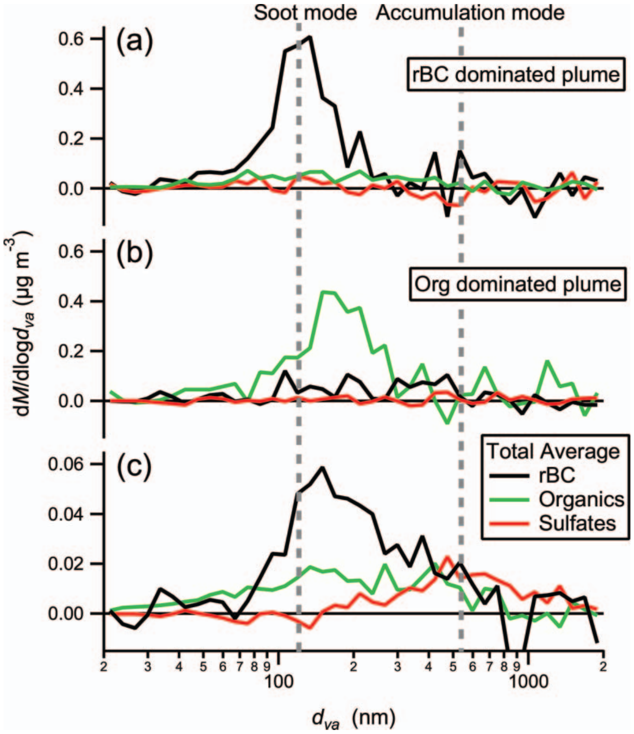

FIG. 9. SP-AMS average size distributions (mass loading versus vacuum aerodynamic diameter) of rBC, organics (Org), and sulfates ($SO_4$) for (a) "rBC dominated" plume (highlighted in Figure 8), (b) "Org dominated" plume, and (c) as an average for the total sampling period.

rBC particles from a relatively local source with little co-emitted nonrefractory material.

The organic particulate mass associated with rBC particles in the "Org dominated" plume peaks at slightly higher $d_{va}$ ∼170 nm. The larger $d_{va}$ observed for the "Org dominated" plume compared with the "rBC dominated" plume is consistent with the condensation of a larger amount of co-emitted organic material onto fractal-like rBC particles causing them to become more spherical. The framework for this interpretation of $d_{va}$ mass distributions, where $d_{va}$ is a function of particle size, shape, and density, has been detailed by Slowik et al. (2007) from laboratory studies. The combined size and chemical information indicates that these 2 plumes likely contain rBC particles coated with primary organic material from one or more local combustion sources.

Figure 9c shows the average PToF-measured particle $d_{va}$ size distributions for the total sampling period. As indicated in Figure 8a, the sulfate component of the measured rBC particles is not correlated with distinct, locally emitted plumes. Therefore, the measured sulfate mass-weighted size distribution ($d_{va}$ ∼ 500 nm) in Figure 9c is a good indicator of the accumulation mode. The accumulation mode represents particles that are least affected by removal mechanisms in the atmosphere and therefore contains particles representative of a wider geographical region (i.e., regional sources). Particles grow into the accumulation mode by condensation and coagulation mechanisms and are typically composed of mixtures of different chemical compositions. Thus, the average $d_{va}$ distributions for rBC in Figure 9c can be interpreted such that most of the ambient rBC measured during this study in an urban environment was from local sources with varying amounts of condensed HOA. Less than 30% of the rBC mass appears to be directly associated with accumulation mode particles, indicative of aged rBC particles.

## REFERENCES

Adachi, K., Chung, S. H., and Buseck, P. R. (2010). Shapes of Soot Aerosol Particles and Implications for Their Effects on Climate. *J. Geophys. Res.*, 115:1–9.

Aiken, A. C., DeCarlo, P. F., and Jimenez, J. L. (2007). Elemental Analysis of Organic Species with Electron Ionization High-Resolution Mass Spectrometry. *Anal. Chem.*, 79:8350–8358.

Allan, J. D., Delia, A. E., Coe, H., Bower, K. N., Alfarra, M. R., Jimenez, J. L., et al. (2004). A Generalised Method for the Extraction of Chemically Resolved Mass Spectra from Aerodyne Aerosol Mass Spectrometer Data. *J. Aerosol Sci.*, 35:909–922.

Bauer, S. E., Menon, S., Koch, D., Bond, T. C., and Tsigaridis, K. (2010). A Global Modeling Study on Carbonaceous Aerosol Microphysical Characteristics and Radiative Effects. *Atmos. Chem. Phys.*, 10:7439–7456.

Baumgardner, D., Kok, G., and Raga, G. (2004). Warming of the Arctic Lower Stratosphere by Light Absorbing Particles. *Geophys. Res. Lett.*, 31:10–13.

Bloomfield, L. A., Geusic, M. E., Freeman, R. R., and Brown, W. L. (1985). Negative and Positive Cluster Ions of Carbon and Silicon. *Chem. Phys. Lett.*, 121: 33–37.

Bond, T. C., Bhardwaj, E., Dong, R., Jogani, R., Jung, S., Roden, C., et al. (2007). Historical Emissions of Black and Organic Carbon Aerosol from Energy-Related Combustion, 1850–2000. *Global Biogeochem. Cy.*, 21:1–16.

Bond, T. C., Streets, D. G., Yarber, K. F., Nelson, S. M., Woo, J.-H., and Kilmont, Z. (2004). A Technology-Based Global Inventory of Black and Organic Carbon Emissions from Combustion. *J. Geophys. Res.*, 109: 1–43.

Canagaratna, M., Jayne, J., Ghertner, D., Herndon, S., Shi, Q., Jimenez, J., et al. (2004). Chase Studies of Particulate Emissions from In-Use New York City Vehicles. *Aerosol Sci. Technol.*, 38:555–573.

Canagaratna, M. R., Jayne, J. T., Jimenez, J. L., Allan, J. D., Alfarra, M. R., Zang, Q., et al. (2007). Chemical and Microphysical Characterization of Ambient Aerosols with the Aerodyne Aerosol Mass Spectrometer. *Mass Spectrom. Rev.*, 26:185–222.

Cross, E. S., Onasch, T. B., Ahern, A., Wrobel, W., Slowik, J. G., Olfert, J., et al. (2010). Soot Particle Studies – Instrument Inter-Comparison – Project Overview. *Aerosol Sci. Technol.*, 44:592–611.

DeCarlo, P. F., Kimmel, J. R., Trimborn, A., Northway, M. J., Jayne, J. T., Aiken, A. C., et al. (2006). Field-Deployable, High-Resolution, Time-of-Flight Aerosol Mass Spectrometer. *Anal. Chem.,* 78:8281–8289.

Dockery, D. W. (2001). Epidemiologic Evidence of Cardiovascular Effects of Particulate Air Pollution. *Environ. Health Persp.,* 109:483–486.

Drewnick, F., Hings, S., DeCarlo, P., Jayne, J., Gonin, M., Fuhrer, K., et al. (2005). A New Time-of-Flight Aerosol Mass Spectrometer (TOF-AMS): Instrument Description and First Field Deployment. *Aerosol Sci. Technol.,* 39:637–658.

Drowart, J., Burns, R. P., DeMaria, G., and Inghram, M. G. (1959). Mass Spectrometric Study of Carbon Vapor. *J. Chem. Phys.,* 31:1131–1132.

Gao, R. S., Schwarz, J. P., Kelly, K. K., Fahey, D. W., Watts, L. A., Thompson, T. L., et al. (2007). A Novel Method for Estimating Light-Scattering Properties of Soot Aerosols Using a Modified Single-Particle Soot Photometer. *Aerosol Sci. Technol.,* 41:125–135.

Grahame, T. J., and Schlesinger, R. B. (2010). Cardiovascular Health and Particulate Vehicular Emissions: A Critical Evaluation of the Evidence. *Air Qual. Atmos. Health,* 3:3–27.

Gysel, M., Laborde, M., Olfert, J. S., Subramanian, R., and Gröhn, A. J. (2011). Effective Density of Aquadag and Fullerene Soot Black Carbon Reference Materials Used for SP2 Calibration. *Atmos. Meas. Tech. Discuss.,* 4:4937–4955.

von Helden, G., Teh Hsu, M., Gotts, N., and Bowers, M. T. (1993). Carbon Cluster Cations with up to 84 Atoms: Structures, Formation Mechanism, and Reactivity. *J. Phys. Chem.*, 97:8182–8192.

Huffman, J., Jayne, J., Drewnick, F., Aiken, A., Onasch, T., Worsnop, D., et al. (2005). Design, Modeling, Optimization, and Experimental Tests of a Particle Beam Width Probe for the Aerodyne Aerosol Mass Spectrometer. *Aerosol Sci. Technol.*, 39:1143–1163.

Jansen, K. L., Larson, T. V., Koenig, J. Q., Mar, T. F., Fields, C., Stewart, J., et al. (2005). Associations Between Health Effects and Particulate Matter and Black Carbon in Subjects with Respiratory Disease. *Environ. Health Persp.,* 113:1741–1746.

Jayne, J. T., Leard, D. C., Zhang, X., Davidovits, P., Smith, K. A., Kolb, C. E., et al. (2000). Development of an Aerosol Mass Spectrometer for Size and Composition Analysis of Submicron Particles. *Aerosol Sci. Technol.,* 33:49–70.

Jimenez, J. L., Jayne, J. T., Shi, Q., Kolb, C. E., Worsnop, D. R., Yourshaw, I., et al. (2003). Ambient Aerosol Sampling Using the Aerodyne Aerosol Mass Spectrometer. *J. Geophys. Res.,* 108:8425.

Kietzmann, H., Rochow, R., Ganteför, G., Eberhardt, W., Vietze, K., Seifert, G., et al. (1998). Electronic Structure of Small Fullerenes: Evidence for the High Stability of C32. *Phys. Rev. Lett.,* 81:5378–5381.

Kimmel, J. R., Farmer, D. K., Cubison, M. J., Sueper, D., Tanner, C., Nemitz, E., et al. (2011). Real-Time Aerosol Mass Spectrometry with Millisecond Resolution. *Int. J. Mass Spectrom.,* 303:15–26.

Lelieveld, J., Crutzen, P. J., Ramanathan, V., Andreae, M. O., Brenninkmeijer, C. M., Campos, T., et al. (2001). The Indian Ocean Experiment: Widespread Air Pollution from South and Southeast Asia. *Science,* 291: 1031–1036.

Matthew, B. M., Middlebrook, A. M., and Onasch, T. B. (2008). Collection Efficiencies in an Aerodyne Aerosol Mass Spectrometer as a Function of Particle Phase for Laboratory Generated Aerosols. *Aerosol Sci. Technol.*, 42:884–898.

McLafferty, F. W., and Turecek, F. (1993). *Interpretation of Mass Spectra*. University Science Books, Mill Valley, CA.

Moteki, N., and Kondo, Y. (2007). Effects of Mixing State on Black Carbon Measurements by Laser-Induced Incandescence. *Aerosol Sci. Technol.,* 41:398–417.

Moteki, N., and Kondo, Y. (2010). Dependence of Laser-Induced Incandescence on Physical Properties of Black Carbon Aerosols: Measurements and Theoretical Interpretation. *Aerosol Sci. Technol.,* 44:663–675.

Murphy, D. M. (2007). The Design of Single Particle Laser Mass Spectrometers. *Mass Spectrom. Rev.,* 26:150–165.

Olfert, J., and Collings, N. (2005). New Method for Particle Mass Classification: The Couette Centrifugal Particle Mass Analyzer. *J. Aerosol Sci.,* 36:1338–1352.

Olfert, J., Reavell, K., Rushton, M., and Collings, N. (2006). The Experimental Transfer Function of the Couette Centrifugal Particle Mass Analyzer. *J. Aerosol Sci.,* 37:1840–1852.

Onasch, T. B., Jayne, J. T., Herndon, S., Worsnop, D. R., Miake-Lye, R. C., Mortimer, I. P., et al. (2009). Chemical Properties of Aircraft Engine Particulate Exhaust Emissions. *J. Propul. Power,* 25:1121–1137.

Paatero, P., and Tapper, U. (1994). Positive Matrix Factorization: A Non-Negative Factor Model with Optimal Utilization of Error Estimates of Data Values. *Environmetrics,* 5:111–126.

Pratt, K. A., and Prather, K. A. (2011). Mass Spectrometry of Atmospheric Aerosols – Recent Developments and Applications, Part II: On-Line Mass Spectrometry Techniques. *Mass Spectrom. Rev.,* 31:17–48.

Ramanathan, V., and Carmichael, G. (2008). Global and Regional Climate Changes Due to Black Carbon. *Nat. Geosci.,* 1:221–227.

Salcedo, D., Onasch, T. B., Aiken, A. C., Williams, L. R., de Foy, B., Cubison, M. J., et al. (2010). Determination of Particulate Lead Using Aerosol Mass Spectrometry: MILAGRO/MCMA-2006 Observations. *Atmos. Chem. Phys.,* 10:5371–5389.

Salcedo, D., Onasch, T. B., Canagaratna, M. R., Dzepina, K., Huffman, J. A., Jayne, J. T., et al. (2007). Technical Note: Use of a Beam Width Probe in an Aerosol Mass Spectrometer to Monitor Particle Collection Efficiency in the field. *Atmos. Chem. Phys.,* 7:549–556.

Schwarz, J. P., Gao, R. S., Fahey, D. W., Thomson, D. S., Watts, L. A., Wilson, J. C., et al. (2006). Single-Particle Measurements of Midlatitude Black Carbon and Light-Scattering Aerosols from the Boundary Layer to the Lower Stratosphere. *J. Geophys. Res.,* 111:1–15.

Schwarz, J. P., Gao, R. S., Spackman, J. R., Watts, L. A., Thomson, D. S., Fahey, D. W., et al. (2008). Measurement of the Mixing State, Mass, and Optical Size of Individual Black Carbon Particles in Urban and Biomass Burning Emissions. *Geophys. Res. Lett.,* 35:1–5.

Schwarz, J. P., Spackman, J. R., Fahey, D. W., Gao, R. S., Lohmann, U., Stier, P., et al. (2008). Coatings and Their Enhancement of Black Carbon Light Absorption in the Tropical Atmosphere. *J. Geophys. Res.,* 113:1–10.

Schwarz, J. P., Spackman, J. R., Gao, R. S., Perring, A. E., Cross, E., Onasch, T. B., et al. (2010). The Detection Efficiency of the Single Particle Soot Photometer. *Aerosol Sci. Technol.,* 44:612–628.

Seinfeld, J. (2008). Atmospheric Science: Black Carbon and Brown Clouds. *Nat. Geosci.,* 1:15–16.

Shiraiwa, M., Kondo, Y., Moteki, N., Takegawa, N., Miyazaki, Y., and Blake, D. R. (2007). Evolution of Mixing State of Black Carbon in Polluted Air from Tokyo. *Geophys. Res. Lett.,* 34:2–6.

Slowik, J., Stainken, K., Davidovits, P., Williams, L., Jayne, J., Kolb, C., et al. (2004). Particle Morphology and Density Characterization by Combined Mobility and Aerodynamic Diameter Measurements. Part 2: Application to Combustion-Generated Soot Aerosols as a Function of Fuel Equivalence Ratio. *Aerosol Sci. Technol.,* 38:1206–1222.

Slowik, J. G., Cross, E. S., Han, J.-H., Kolucki, J., Davidovits, P., Williams, L. R., et al. (2007). Measurements of Morphology Changes of Fractal Soot Particles Using Coating and Denuding Experiments: Implications for Optical Absorption and Atmospheric Lifetime. *Aerosol Sci. Technol.,* 41: 734–750.

Spencer, M. K., Hammond, M. R., and Zare, R. N. (2008). Laser Mass Spectrometric Detection of Extraterrestrial Aromatic Molecules: Mini-Review and Examination of Pulsed Heating Effects. *Proc. Nat. Acad. Sci. USA.,* 105:18096–18101.

Stephens, M., Turner, N., and Sandberg, J. (2003). Particle Identification by Laser-Induced Incandescence in a Solid-State Laser Cavity. *Appl. Optics,* 42:3726–3736.

Takegawa, N., Miyazaki, Y., Kondo, Y., Komazaki, Y., Miyakawa, T., Jimenez, J. L., et al. (2005). Characterization of an Aerodyne Aerosol Mass Spectrometer (AMS): Intercomparison with Other Aerosol Instruments. *Aerosol Sci. Technol.,* 39:760–770.

Ulbrich, I. M., Canagaratna, M. R., Zhang, Q., Worsnop, D. R., and Jimenez, J. L. (2009). Interpretation of Organic Components from Positive Matrix Factorization of Aerosol Mass Spectrometric Data. *Atmos. Chem. Phys.*, 9:2891–2918.

Vékey, K. (1996). Internal Energy Effects in Mass Spectrometry. *J. Mass Spectrom.,* 31:445–463.

Wilson, K. R., Jimenez-Cruz, M., Nicolas, C., Belau, L., Leone, S. R., and Ahmed, M. (2006). Thermal Vaporization of Biological Nanoparticles: Fragment-Free Vacuum Ultraviolet Photoionization Mass Spectra of Tryptophan, Phenylalanine-Glycine-Glycine, and Beta-Carotene. *J. Phys. Chem. A,* 110:2106–2113.